

# A Spectral-Element Discontinuous Galerkin Lattice Boltzmann Method for Incompressible Flows

Misun Min<sup>1</sup>

*Mathematics and Computer Science Division, Argonne National Laboratory,  
Argonne, IL 60439, USA*

Taehun Lee<sup>† 2</sup>

*Department of Mechanical Engineering, City College of City University of New  
York, New York, NY 10031, USA*

---

## Abstract

We present a spectral-element discontinuous Galerkin lattice Boltzmann method for solving single-phase incompressible flows. Decoupling the collision step from the streaming step offers numerical stability at high Reynolds numbers. In the streaming step, we employ high-order spectral-element discretizations using a tensor product basis of one-dimensional Lagrange interpolation polynomials based on Gauss-Lobatto-Legendre grids. Our scheme is cost-effective with a fully diagonal mass matrix, advancing time integration with the fourth-order Runge-Kutta method. We present a consistent boundary treatment allowing us to use both central and Lax-Friedrichs fluxes for the numerical flux in the discontinuous Galerkin approach. We present two benchmark cases: lid-driven cavity flows for  $Re=400-5000$  and flows around an impulsively started cylinder for  $Re=550-9500$ . Computational results are compared with those of other theoretical, experimental, and computational work that used a multigrid method, a vortex method, and a spectral element model.

*Key words:* Lattice Boltzmann Method, Spectral Element Method, Discontinuous Galerkin Method

---

---

<sup>1</sup> E-mail: mmin@mcs.anl.gov. This author was supported by the Office of Advanced Scientific Computing Research, Office of Science, U.S. Department of Energy, under Contract DE-AC02-06CH11357.

<sup>2</sup> <sup>†</sup> Corresponding author. E-mail: thlee@ccny.cuny.edu. This author was supported by the National Science Foundation grant DMS-0811046.

## 1 Introduction

The lattice Boltzmann method (LBM) has been successfully applied to many computational fluid dynamics problems over the past two decades [1–3]. LBM can offer highly parallel algorithms and accurate solutions because of the use of uniform Cartesian meshes, which make the streaming of the particle distribution function as the exact solution of linear advection equation. Severe limitations arise, however, from its inherent instability at high Reynolds number ( $Re$ ) and the use of uniform structured grids. These two aspects are closely related to each other in that the lattice Boltzmann equation (LBE) is a discretized form of the discrete Boltzmann equation (DBE) along characteristics, and thus the time and space discretizations are strongly coupled. Since He and Luo [4] and Abe [5] demonstrated that the discretization of physical space does not necessarily need to couple with the discretization of momentum space, several efforts have been made to address the treatment of curved or irregular boundaries and the control of mesh resolution at desirable regions, and significant progress has been achieved in recent years to overcome the limitations of LBM. Cao et al. [6] indicated that the conventional LBM is a special finite difference discretization of the kinetic equation of the discrete velocity distribution function, and thus LBE can be solved on nonuniform grids using a semi-implicit collision scheme. With a rigorous foundation established, various numerical methods have been applied directly to the discrete Boltzmann equation (DBE) using finite difference (FD) [7–13], finite volume (FV) [14–18], finite element (FE) [19–21], and spectral-element discontinuous Galerkin (SEDG) methods [22,23].

FD-LBM is a straightforward generalization of the conventional LBM at non-unit CFL number [24] and offers flexibility in the choice of time-stepping methods. The perfect shift in the conventional LBM is a special case of FD-LBM at unit CFL number. The simple Cartesian grid structure for FD-LBM offers ease of implementation but complicates accurate treatment of curved boundaries, causing unwanted velocity slip and mass and momentum conservation errors [25,26]. The spatial approximation of FV-LBM uses purely local approximation in space and imposes no conditions on the grid structure; thus, the approach is suitable for dealing with complex geometries. From the divergence theorem, the flux term of DBE becomes surface integral, requiring local reconstruction of the fluxes at the boundaries. However, when we need to increase the order of accuracy, a high-order reconstruction of the solution values at the interface destroys the geometric flexibility [27], which makes high-order accuracy on unstructured grids a challenge. On the contrary, FE-LBM allows higher-order approximation simply by adding additional degrees of freedom to the element, while retaining geometric flexibility. In FE-LBM, the solution is continuous on the nodes along the faces of the elements shared by the neighboring elements, which essentially introduces the globally defined basis and

test functions. The inversion of global mass matrix can be expensive, however, when a fully explicit time-stepping method is employed.

SEDG-LBM uses the local element-based basis, which makes the mass matrix local and thus can be inverted at little cost. Like the finite-volume method it also satisfies the governing equation by introducing numerical fluxes, but it is able to achieve high-order accuracy on general grids [27].

In this paper, we present SEDG-LBM using quadrilateral elements based on Gauss-Lobatto-Legendre grids, for which the two-dimensional mass matrix becomes a complete diagonal matrix whose inversion is trivial. High-order discretization is used with explicit time-stepping. In our SEDG-LBM, the SEDG approximation is applied to the streaming step after the collision step is completed, whereas the SEDG-LBMs in [22,23] are applied to the complete DBE. Our approach avoids the severe time-step restriction caused by small values of the relaxation time and enables us to investigate flows at higher  $Re$ . Both central and upwind numerical fluxes are implemented for benchmark problems. In [22,23], only the upwind-biased numerical flux was considered, largely because of the numerical instability with the central flux. For the particle distribution function that enters into the computational domain, a boundary condition needs to be provided. The most popular wall boundary condition is the bounce-back scheme [28], in which the incoming particle distribution function into the domain takes the value of the outgoing particle distribution function in the opposite direction. In [23], the bounce-back rule was imposed strongly on the incoming particle distribution function after each time step. In the present work, the bounce-back scheme is implemented in a weak sense through the numerical flux, which is consistent with the overall numerical procedure inside the computational domain.

The paper is organized as follows. In Section 2, we present the LBE for the incompressible flows and the SEDG approximation applied to the LBE. Spatial and temporal discretizations are detailed, and numerical fluxes for wall boundary conditions are discussed. Section 3 is devoted to validation of our SEDG-LBM. The physics of lid-driven cavity flows and impulsively started flows past a circular cylinder are studied. Conclusions are given in Section 4.

## 2 Formulation

We describe LBM including two steps: collision and streaming. For the streaming step, we examine a discontinuous Galerkin approach based on spectral element discretizations using quadrilateral meshes in two dimensions. We construct numerical fluxes and present a consistent treatment for imposing boundary conditions with the central and Lax-Friedrichs fluxes. Spatial and temporal

discretizations are discussed in detail.

### 2.1 Lattice Boltzmann Equation

We consider the discrete Boltzmann equation with the Bhatnagar-Gross-Krook collision operator [29]

$$\frac{\partial f_\alpha}{\partial t} + \mathbf{e}_\alpha \cdot \nabla f_\alpha = -\frac{f_\alpha - f_\alpha^{eq}}{\lambda} \quad \text{on } \Omega \quad \text{for } \alpha = 0, 1, \dots, N_\alpha, \quad (1)$$

where  $f_\alpha$  is the particle distribution function defined in the direction of the microscopic particle velocity  $\mathbf{e}_\alpha$ ,  $\lambda$  is the relaxation time, and  $N_\alpha$  is the number of microscopic velocity. The local equilibrium distribution function is given by

$$f_\alpha^{eq} = t_\alpha \rho \left[ 1 + \frac{\mathbf{e}_\alpha \cdot \mathbf{u}}{c_s^2} + \frac{(\mathbf{e}_\alpha \cdot \mathbf{u})^2}{2c_s^4} - \frac{(\mathbf{u} \cdot \mathbf{u})}{2c_s^2} \right], \quad (2)$$

where  $t_\alpha$  is the weight,  $\rho$  is the density,  $\mathbf{u}$  is the macroscopic velocity, and  $c_s$  is the speed of sound [30].

Then the discrete form of the DBE in Eq. (1) along characteristics over the time step  $\delta t$ , called the LBE, are obtained as

$$f_\alpha(\mathbf{x}, t) - f_\alpha(\mathbf{x} - \mathbf{e}_\alpha \delta t, t - \delta t) = - \int_{t-\delta t}^t \frac{f_\alpha - f_\alpha^{eq}}{\lambda} dt'. \quad (3)$$

The time integration over  $[t - \delta t, t]$  is coupled with the space integration in  $[\mathbf{x} - \mathbf{e}_\alpha \delta t, \mathbf{x}]$ . Taking a second-order approximation by the trapezoidal rule for the integration in the right-hand side of Eq. (3), we have

$$\begin{aligned} & f_\alpha(\mathbf{x}, t) - f_\alpha(\mathbf{x} - \mathbf{e}_\alpha \delta t, t - \delta t) \\ &= -\frac{f_\alpha - f_\alpha^{eq}}{2\tau} \Big|_{(\mathbf{x} - \mathbf{e}_\alpha \delta t, t - \delta t)} - \frac{f_\alpha - f_\alpha^{eq}}{2\tau} \Big|_{(\mathbf{x}, t)}, \end{aligned} \quad (4)$$

where the nondimensional relaxation time is  $\tau = \lambda/\delta t$  with relation to the kinematic viscosity by  $\nu = \tau c_s^2 \delta t$ .

Here, we introduce a modified particle distribution function  $\bar{f}_\alpha$  and its corresponding equilibrium distribution function  $\bar{f}_\alpha^{eq}$  in order to facilitate computation [31]:

$$\bar{f}_\alpha = f_\alpha + \frac{f_\alpha - f_\alpha^{eq}}{2\tau} \quad \text{and} \quad \bar{f}_\alpha^{eq} = f_\alpha^{eq}. \quad (5)$$

The density and momentum can be computed by taking moments as follows:

$$\rho = \sum_{\alpha=0}^{N_\alpha} f_\alpha = \sum_{\alpha=0}^{N_\alpha} \bar{f}_\alpha, \quad \text{and} \quad \rho \mathbf{u} = \sum_{\alpha=0}^{N_\alpha} \mathbf{e}_\alpha f_\alpha = \sum_{\alpha=0}^{N_\alpha} \mathbf{e}_\alpha \bar{f}_\alpha. \quad (6)$$

Then Eq. (4) can be recast in a simpler form in terms of the modified particle distribution function:

$$\bar{f}_\alpha(\mathbf{x}, t) - \bar{f}_\alpha(\mathbf{x} - \mathbf{e}_\alpha \delta t, t - \delta t) = -\frac{1}{\tau + 0.5} \left( \bar{f}_\alpha - \bar{f}_\alpha^{eq} \right) |_{(\mathbf{x} - \mathbf{e}_\alpha \delta t, t - \delta t)}. \quad (7)$$

Note that although Eq. (7) appears to be explicit in time, it is fully implicit for the relaxation term.

We solve Eq. (7) in two steps:

- Collision:

$$\begin{aligned} & \bar{f}_\alpha(\mathbf{x} - \mathbf{e}_\alpha \delta t, t - \delta t) \\ & := \bar{f}_\alpha(\mathbf{x} - \mathbf{e}_\alpha \delta t, t - \delta t) - \frac{1}{\tau + 0.5} \left( \bar{f}_\alpha - \bar{f}_\alpha^{eq} \right) |_{(\mathbf{x} - \mathbf{e}_\alpha \delta t, t - \delta t)}, \end{aligned} \quad (8)$$

- Streaming:

$$\bar{f}_\alpha(\mathbf{x}, t) = \bar{f}_\alpha(\mathbf{x} - \mathbf{e}_\alpha \delta t, t - \delta t). \quad (9)$$

The streaming step can be expressed as a solution of the pure advection equation

$$\frac{\partial \bar{f}_\alpha}{\partial t} + \mathbf{e}_\alpha \cdot \nabla \bar{f}_\alpha = 0. \quad (10)$$

In the conventional LBM, the grid points coincide with the lattice points, and the streaming step expressed by Eq. (9) becomes a perfect shift but when using unstructured grids the accuracy for the streaming step depends on the approximation order of the scheme used.

In the next section, we discuss discretizations and algorithms for solving the advection equation using a spectral element discontinuous Galerkin approach with Runge-Kutta time-stepping. Combined with the collision step based on the choice of the two-dimensional 9-velocity lattice [30], we complete the description of our SEDG-LBM.

## 2.2 Discontinuous Galerkin Spectral Element Method

We begin section with a weak formulation of the advection equation, Eq. (10), using a discontinuous Galerkin approach introducing a flux vector. Spectral element discretizations, numerical flux with boundary condition implementation, and time integration are discussed.

### 2.2.1 Weak Formulation for the Discontinuous Galerkin Method

We use a multidomain approach for solving the advection equation, Eq. (10). We consider a nonoverlapping element  $\Omega^e$  such that  $\Omega = \cup_{e=1}^E \Omega^e$ . We introduce a flux vector defined as  $\mathbf{F}_\alpha(\bar{f}) = \mathbf{e}_\alpha \bar{f}_\alpha$  for the velocity vector  $\mathbf{e}_\alpha = (e_{\alpha x}, e_{\alpha y})$ . Then Eq. (10) defined on  $\Omega$  can be written as

$$\frac{\partial \bar{f}_\alpha}{\partial t} + \nabla \cdot \mathbf{F}_\alpha(\bar{f}) = 0. \quad (11)$$

Eq. (11) can be recast in an equivalent variational form as

$$\left( \frac{\partial \bar{f}_\alpha}{\partial t} + \nabla \cdot \mathbf{F}_\alpha(\bar{f}), \phi \right)_{\Omega^e} = 0, \quad (12)$$

where  $\phi$  is a local test function. Integrating by parts of Eq. (12), we obtain

$$\int_{\Omega^e} \phi \frac{\partial \bar{f}_\alpha}{\partial t} d\Omega - \int_{\Omega^e} \mathbf{F}_\alpha(\bar{f}) \cdot \nabla \phi d\Omega = - \int_{\partial \Omega^e} \phi \mathbf{n} \cdot \mathbf{F}_\alpha(\bar{f}) d\bar{\Omega}, \quad (13)$$

where  $\bar{\Omega}$  represents the surface boundary of the element  $\Omega^e$  (i.e.,  $\partial \Omega^e$ ) and  $\mathbf{n} = (n_x, n_y)$  is the unit normal vector pointing outward. Here we introduce a numerical flux  $\mathbf{F}^*$ , which is a function of the local solution  $\bar{f}$  and the neighboring solution  $\bar{f}^+$  at the interfaces between neighboring elements. The numerical flux combines the two solutions that are allowed to be different at the neighboring element interfaces. The analytic flux  $\mathbf{F}_\alpha(\bar{f})$  is replaced by the numerical flux  $\mathbf{F}_\alpha^*(\bar{f})$ :

$$\int_{\Omega^e} \phi \frac{\partial \bar{f}_\alpha}{\partial t} d\Omega - \int_{\Omega^e} \mathbf{F}_\alpha(\bar{f}) \cdot \nabla \phi d\Omega = - \int_{\partial \Omega^e} \phi \mathbf{n} \cdot \mathbf{F}_\alpha^*(\bar{f}) d\bar{\Omega}. \quad (14)$$

Integrating by parts of Eq. (14) again, we obtain the final form of the weak formulation as follows:

$$\left( \frac{\partial \bar{f}_\alpha}{\partial t} + \nabla \cdot \mathbf{F}_\alpha(\bar{f}), \phi \right)_{\Omega^e} = \left( \mathbf{n} \cdot [\mathbf{F}_\alpha(\bar{f}) - \mathbf{F}_\alpha^*(\bar{f})], \phi \right)_{\partial\Omega^e}. \quad (15)$$

### 2.2.2 Numerical Fluxes for the Discontinuous Galerkin Method

Here we define two different numerical fluxes, central and Lax-Friedrichs fluxes, for  $\mathbf{F}_\alpha^*(\bar{f}) = \mathbf{F}_\alpha^*(\bar{f}, \bar{f}^+)$ , which we used for our simulations.

(i) *Central Flux:* For the central flux given by

$$\mathbf{F}_\alpha^*(\bar{f}, \bar{f}^+) = \frac{1}{2} [\mathbf{F}_\alpha(\bar{f}) + \mathbf{F}_\alpha(\bar{f}^+)], \quad (16)$$

we have the following form in the integrand of Eq. (15):

$$\mathbf{n} \cdot (\mathbf{F}_\alpha - \mathbf{F}_\alpha^*) = \frac{1}{2} (\mathbf{n} \cdot \mathbf{e}_\alpha) [\bar{f}_\alpha - \bar{f}_\alpha^+] = \frac{1}{2} (n_x e_{\alpha x} + n_y e_{\alpha y}) [\bar{f}_\alpha - \bar{f}_\alpha^+]. \quad (17)$$

At the interfaces, the normal vectors hold:  $n_x = -n_x^+$  and  $n_y = -n_y^+$ . However, the velocity vector components are always fixed in the neighboring element for each  $\mathbf{e}_\alpha$ . Thus Eq. (17) can be separated into two components: one for local component and the other for neighboring component with "+" :

$$\mathbf{n} \cdot (\mathbf{F}_\alpha - \mathbf{F}_\alpha^*) = \frac{1}{2} [(n_x e_{\alpha x} + n_y e_{\alpha y}) \bar{f}_\alpha + (n_x^+ e_{\alpha x} + n_y^+ e_{\alpha y}) \bar{f}_\alpha^+]. \quad (18)$$

(ii) *Lax-Friedrichs Flux:* For the Lax-Friedrichs flux [27,32,33], we have

$$\mathbf{F}_\alpha^*(\bar{f}, \bar{f}^+) = \frac{1}{2} [\mathbf{F}_\alpha(\bar{f}) + \mathbf{F}_\alpha(\bar{f}^+) + |\Lambda|(\bar{f}_\alpha - \bar{f}_\alpha^+) \mathbf{n}], \quad (19)$$

where  $\Lambda = \max \left( \mathbf{n} \cdot \frac{\partial \mathbf{F}}{\partial f} \right) = \mathbf{n} \cdot \mathbf{e}_\alpha$ . Then, since we have

$$\mathbf{n} \cdot (\mathbf{F}_\alpha - \mathbf{F}_\alpha^*) = \frac{1}{2} (\mathbf{n} \cdot \mathbf{e}_\alpha - |\mathbf{n} \cdot \mathbf{e}_\alpha|) [\bar{f}_\alpha - \bar{f}_\alpha^+], \quad (20)$$

the equation can be simplified as

$$\mathbf{n} \cdot (\mathbf{F}_\alpha - \mathbf{F}_\alpha^*) = \begin{cases} (\mathbf{n} \cdot \mathbf{e}_\alpha) [\bar{f}_\alpha - \bar{f}_\alpha^+] & \text{for } \mathbf{n} \cdot \mathbf{e}_\alpha < 0, \\ 0 & \text{for } \mathbf{n} \cdot \mathbf{e}_\alpha \geq 0. \end{cases} \quad (21)$$

In the similar manner as in (18), for the case of  $\mathbf{n} \cdot \mathbf{e}_\alpha < 0$ , we can write

$$\mathbf{n} \cdot (\mathbf{F}_\alpha - \mathbf{F}_\alpha^*) = (n_x e_{\alpha x} + n_y e_{\alpha y}) \bar{f}_\alpha + (n_x^+ e_{\alpha x} + n_y^+ e_{\alpha y}) \bar{f}_\alpha^+. \quad (22)$$

### 2.2.3 Boundary Conditions

The wall and moving wall boundaries are weakly imposed through the numerical fluxes. For outgoing flows  $\mathbf{e}_\alpha \cdot \mathbf{n} > 0$ , the flux difference is set to be  $\bar{f}_\alpha - \bar{f}_\alpha^+ = 0$ . For incoming flows  $\mathbf{e}_\alpha \cdot \mathbf{n} < 0$ , we apply boundary conditions through  $\bar{f}_\alpha - \bar{f}_\alpha^+ = \bar{f}_\alpha - \bar{f}_{\alpha^*}^+ - 2t_\alpha(\mathbf{e}_\alpha \cdot \mathbf{u}_b)/c_s^2$ , where  $\alpha^*$  indicates the velocity component in the opposite direction of  $\alpha$  and  $\mathbf{u}_b$  is the velocity defined at the boundaries. The detailed expression for the flux difference in Eqs. (17) and (21) can be written as

$$\begin{aligned} \text{if } \mathbf{e}_1 \cdot \mathbf{n} < 0 \ (\Leftrightarrow \mathbf{e}_3 \cdot \mathbf{n} > 0); \quad & \bar{f}_1 - \bar{f}_1^+ = [\bar{f}_1 - \bar{f}_3^+] - 2t_1(\mathbf{e}_1 \cdot \mathbf{u}_b)/c_s^2, \\ & \bar{f}_3 - \bar{f}_3^+ = [\bar{f}_3 - \bar{f}_1^+] = 0, \end{aligned}$$

$$\begin{aligned} \text{if } \mathbf{e}_2 \cdot \mathbf{n} < 0 \ (\Leftrightarrow \mathbf{e}_4 \cdot \mathbf{n} > 0); \quad & \bar{f}_2 - \bar{f}_2^+ = [\bar{f}_2 - \bar{f}_4^+] - 2t_2(\mathbf{e}_2 \cdot \mathbf{u}_b)/c_s^2, \\ & \bar{f}_4 - \bar{f}_4^+ = [\bar{f}_4 - \bar{f}_2^+] = 0, \end{aligned}$$

$$\begin{aligned} \text{if } \mathbf{e}_3 \cdot \mathbf{n} < 0 \ (\Leftrightarrow \mathbf{e}_1 \cdot \mathbf{n} > 0); \quad & \bar{f}_3 - \bar{f}_3^+ = [\bar{f}_3 - \bar{f}_1^+] - 2t_3(\mathbf{e}_3 \cdot \mathbf{u}_b)/c_s^2, \\ & \bar{f}_1 - \bar{f}_1^+ = [\bar{f}_1 - \bar{f}_3^+] = 0, \end{aligned}$$

$$\begin{aligned} \text{if } \mathbf{e}_4 \cdot \mathbf{n} < 0 \ (\Leftrightarrow \mathbf{e}_2 \cdot \mathbf{n} > 0); \quad & \bar{f}_4 - \bar{f}_4^+ = [\bar{f}_4 - \bar{f}_2^+] - 2t_4(\mathbf{e}_4 \cdot \mathbf{u}_b)/c_s^2, \\ & \bar{f}_2 - \bar{f}_2^+ = [\bar{f}_2 - \bar{f}_4^+] = 0, \end{aligned}$$

$$\begin{aligned} \text{if } \mathbf{e}_5 \cdot \mathbf{n} < 0 \ (\Leftrightarrow \mathbf{e}_7 \cdot \mathbf{n} > 0); \quad & \bar{f}_5 - \bar{f}_5^+ = [\bar{f}_5 - \bar{f}_7^+] - 2t_5(\mathbf{e}_5 \cdot \mathbf{u}_b)/c_s^2, \\ & \bar{f}_7 - \bar{f}_7^+ = [\bar{f}_7 - \bar{f}_5^+] = 0, \end{aligned}$$

$$\begin{aligned} \text{if } \mathbf{e}_6 \cdot \mathbf{n} < 0 \ (\Leftrightarrow \mathbf{e}_8 \cdot \mathbf{n} > 0); \quad & \bar{f}_6 - \bar{f}_6^+ = [\bar{f}_6 - \bar{f}_8^+] - 2t_6(\mathbf{e}_6 \cdot \mathbf{u}_b)/c_s^2, \\ & \bar{f}_8 - \bar{f}_8^+ = [\bar{f}_8 - \bar{f}_6^+] = 0, \end{aligned}$$

$$\begin{aligned} \text{if } \mathbf{e}_7 \cdot \mathbf{n} < 0 \ (\Leftrightarrow \mathbf{e}_5 \cdot \mathbf{n} > 0); \quad & \bar{f}_7 - \bar{f}_7^+ = [\bar{f}_7 - \bar{f}_5^+] - 2t_7(\mathbf{e}_7 \cdot \mathbf{u}_b)/c_s^2, \\ & \bar{f}_5 - \bar{f}_5^+ = [\bar{f}_5 - \bar{f}_7^+] = 0, \end{aligned}$$

$$\begin{aligned} \text{if } \mathbf{e}_8 \cdot \mathbf{n} < 0 \ (\Leftrightarrow \mathbf{e}_3 \cdot \mathbf{n} > 0); \quad & \bar{f}_8 - \bar{f}_8^+ = [\bar{f}_8 - \bar{f}_6^+] - 2t_8(\mathbf{e}_8 \cdot \mathbf{u}_b)/c_s^2, \\ & \bar{f}_6 - \bar{f}_6^+ = [\bar{f}_6 - \bar{f}_8^+] = 0, \end{aligned}$$

where  $t_\alpha$  is the weight with  $t_0 = 4/9$ ,  $t_\alpha(\alpha = 1, 3, 5, 7) = 1/9$  and  $t_\alpha(\alpha = 2, 4, 6, 8) = 1/36$  for the case of the 9-velocity lattice [30].



### 2.2.4 Spectral Element Basis, Differentiation, and Integration

Here we describe a set of one-dimensional discretization grids and its associated Lagrangian basis, differentiation matrix, and quadrature weights. We consider the ordered set of  $N + 1$  Gauss-Lobatto-Legendre (GLL) quadrature nodes  $\{\xi_0, \xi_1, \dots, \xi_N\}$  that are solution of the equation

$$(1 - \xi^2)L'_N(\xi) = 0, \quad \xi \in [-1, 1], \quad (23)$$

where  $L'_N(\xi)$  is the derivative of the  $N$ th order Legendre polynomial  $L_N(\xi)$ . Our one-dimensional Lagrange interpolation basis with the GLL grids is given by

$$l_i(\xi) = \frac{-1}{N(N+1)} \frac{(1 - \xi^2)L'_N(\xi)}{(\xi - \xi_i)L'_N(\xi_i)}, \quad 0 \leq i \leq N, \quad \xi \in [-1, 1], \quad (24)$$

which satisfies  $l_i(\xi_j) = \delta_{ij}$ , where  $\delta_{ij}$  is the Kronecker delta. It immediately provides the one-dimensional differentiation matrix  $\hat{D}$  at the GLL grids  $\xi_k$  given by

$$\hat{D}_{ki} = \frac{\partial l_i(\xi_k)}{\partial \xi} = l'_i(\xi_k), \quad (25)$$

whose the explicit form is shown in [34,35]. The quadrature rule for the inner product associated with the GLL grids is defined as

$$(f, g)_{[a,b]} = \int_a^b f(x)g(x)dx = \int_{-1}^1 f(\xi)g(\xi)J(\xi)d\xi \approx \sum_{k=0}^N f(\xi_k)g(\xi_k)w_k J_k, \quad (26)$$

where the quadrature weights are defined by  $w_k = 2[N(N+1)L_N^2(\xi_k)]^{-1}$  and the local Jacobian for the transformation between  $[a, b]$  and  $[-1, 1]$  is  $J(\xi) = \frac{dx}{d\xi}$  and  $J_k$  represents  $J(\xi_k)$ .

### 2.2.5 Spectral Element Discretizations

Now we consider our computational domain  $\Omega$  in two-dimensional space. Each  $(x, y) \in \Omega^e$  is mapped on the reference domain,  $(\xi, \eta) \in I = [-1, 1]^2$ , through a Gordon-Hall mapping [34]. The tensor-product structure of the reference element  $I$  allows us to define a two-dimensional basis as  $\psi_{ij}(\xi, \eta) = l_i(\xi(x))l_j(\eta(y))$ , or simply  $\psi_{ij}$ .

We seek a local approximate solution in  $\Omega^e$  defined by the finite expansion of the tensor product basis  $\psi_{ij}(\xi, \eta)$  as

$$\bar{f}_\alpha^N := \bar{f}_\alpha^N(x, y, t) = \sum_{i,j=0}^N (\bar{f}_\alpha^N)_{ij} \psi_{ij}(\xi, \eta), \quad (27)$$

where  $(\bar{f}_\alpha^N)_{ij} = \bar{f}_\alpha^N(x_i, y_j, t)$ , that is, the nodal values of the approximate solution  $\bar{f}_\alpha^N$  at time  $t$  on the tensor product of the one-dimensional GLL quadrature nodes,  $(\xi_i, \eta_j)$  [34].

For derivatives, we have

$$\frac{\partial \bar{f}_\alpha^N}{\partial t} = \sum_{i,j=0}^N \frac{d(\bar{f}_\alpha^N)_{ij}}{dt} \psi_{ij}(\xi, \eta), \quad (28)$$

$$\frac{\partial \bar{f}_\alpha^N}{\partial x} = \sum_{i,j=0}^N (\bar{f}_\alpha^N)_{ij} \frac{\partial \psi_{ij}}{\partial x}(\xi, \eta) = \sum_{i,j=0}^N (\bar{f}_\alpha^N)_{ij} \left( \frac{\partial \psi_{ij}}{\partial \xi} \frac{\partial \xi}{\partial x} + \frac{\partial \psi_{ij}}{\partial \eta} \frac{\partial \eta}{\partial x} \right), \quad (29)$$

$$\frac{\partial \bar{f}_\alpha^N}{\partial y} = \sum_{i,j=0}^N (\bar{f}_\alpha^N)_{ij} \frac{\partial \psi_{ij}}{\partial y}(\xi, \eta) = \sum_{i,j=0}^N (\bar{f}_\alpha^N)_{ij} \left( \frac{\partial \psi_{ij}}{\partial \xi} \frac{\partial \xi}{\partial y} + \frac{\partial \psi_{ij}}{\partial \eta} \frac{\partial \eta}{\partial y} \right), \quad (30)$$

where we can compute the geometric terms pointwise by

$$\frac{\partial \xi}{\partial x} = \frac{1}{J} \frac{\partial y}{\partial \eta}, \quad \frac{\partial \eta}{\partial x} = -\frac{1}{J} \frac{\partial y}{\partial \xi}, \quad \frac{\partial \xi}{\partial y} = -\frac{1}{J} \frac{\partial x}{\partial \eta}, \quad \frac{\partial \eta}{\partial y} = \frac{1}{J} \frac{\partial x}{\partial \xi}, \quad (31)$$

with the Jacobian  $J = \left( \frac{\partial x}{\partial \xi} \frac{\partial y}{\partial \eta} - \frac{\partial x}{\partial \eta} \frac{\partial y}{\partial \xi} \right)$  from the following relation:

$$\begin{pmatrix} \frac{\partial \xi}{\partial x} & \frac{\partial \xi}{\partial y} \\ \frac{\partial \eta}{\partial x} & \frac{\partial \eta}{\partial y} \end{pmatrix} \begin{pmatrix} \frac{\partial x}{\partial \xi} & \frac{\partial x}{\partial \eta} \\ \frac{\partial y}{\partial \xi} & \frac{\partial y}{\partial \eta} \end{pmatrix} \equiv \begin{pmatrix} 1 & 0 \\ 0 & 1 \end{pmatrix}. \quad (32)$$

We recall the weak formulation Eq. (15) and plug Eqs. (27)-(30) into it, with a test function chosen from the tensor product basis, namely,  $\phi := \psi_{i\hat{j}}$ . Then we have the following components in the discretized weak form:

$$\begin{aligned} & \frac{d(\bar{f}_\alpha^N)_{ij}}{dt} (\psi_{ij}, \psi_{i\hat{j}})_{\Omega^e} + e_{\alpha x} (\bar{f}_\alpha^N)_{ij} \left( \frac{\partial \psi_{ij}}{\partial x}, \psi_{i\hat{j}} \right)_{\Omega^e} \\ & + e_{\alpha y} (\bar{f}_\alpha^N)_{ij} \left( \frac{\partial \psi_{ij}}{\partial y}, \psi_{i\hat{j}} \right)_{\Omega^e} = (\mathbf{n} \cdot [\mathbf{F}(\bar{f}_\alpha^N)_{ij} - \mathbf{F}^*(\bar{f}_\alpha^N)_{ij}], \psi_{i\hat{j}})_{\partial \Omega^e}. \end{aligned} \quad (33)$$

Applying the Gauss quadrature rule to Eq. (33), we obtain the mass and stiffness matrices in two dimensions. For the mass matrix, we have

$$\begin{aligned}\mathbf{M} &= (\psi_{ij}, \psi_{\hat{i}\hat{j}})_{\Omega^e} = \sum_{k=0}^N \sum_{m=0}^N l_i(\xi_k) l_{\hat{i}}(\xi_k) l_j(\eta_m) l_{\hat{j}}(\eta_m) w_k w_m J_{km} \\ &= \hat{M} \otimes \hat{M},\end{aligned}\quad (34)$$

where  $J_{km}$  represent the value at each node in a local element for the Jacobian  $J$ . Note that we have

$$\hat{M}_{ij} = \sum_{k=0}^N l_i(\xi_k) l_{\hat{i}}(\xi_k) w_k J_k = \text{diag}(w_i J_i), \quad (35)$$

which is the one-dimensional diagonal mass matrix as in Eq. (26). Its tensor product form is also a complete diagonal matrix in two dimensions. The stiffness matrices are also represented in a tensor product form of the one-dimensional differentiation matrix  $\hat{D}$  in Eq. (25) as

$$\begin{aligned}\mathbf{D}_x &= \left( \frac{\partial \psi_{ij}}{\partial x}, \psi_{\hat{i}\hat{j}} \right) = \sum_{k=0}^N \sum_{m=0}^N l'_i(\xi_k) G_{km}^{\xi x} l_{\hat{i}}(\xi_k) l_j(\eta_m) l_{\hat{j}}(\eta_m) w_k w_m J_{km} \\ &\quad + \sum_{k=0}^N \sum_{m=0}^N l_i(\xi_k) l_{\hat{i}}(\xi_k) l'_j(\eta_m) G_{km}^{\eta x} l_{\hat{j}}(\eta_m) w_k w_m J_{km} \\ &= G^{\xi x} [\hat{M} \otimes \hat{M} \hat{D}] + G^{\eta x} [\hat{M} \hat{D} \otimes \hat{M}],\end{aligned}\quad (36)$$

$$\begin{aligned}\mathbf{D}_y &= \left( \frac{\partial \psi_{ij}}{\partial y}, \psi_{\hat{i}\hat{j}} \right) = \sum_{k=0}^N \sum_{m=0}^N l'_i(\xi_k) G_{km}^{\xi y} l_{\hat{i}}(\xi_k) l_j(\eta_m) l_{\hat{j}}(\eta_m) w_k w_m J_{km} \\ &\quad + \sum_{k=0}^N \sum_{m=0}^N l_i(\xi_k) l_{\hat{i}}(\xi_k) l'_j(\eta_m) G_{km}^{\eta y} l_{\hat{j}}(\eta_m) w_k w_m J_{km} \\ &= G^{\xi y} [\hat{M} \otimes \hat{M} \hat{D}] + G^{\eta y} [\hat{M} \hat{D} \otimes \hat{M}],\end{aligned}\quad (37)$$

where  $G^{\xi x} = \text{diag}(G_{km}^{\xi x})$ ,  $G^{\xi y} = \text{diag}(G_{km}^{\xi y})$ ,  $G^{\eta x} = \text{diag}(G_{km}^{\eta x})$ , and  $G^{\eta y} = \text{diag}(G_{km}^{\eta y})$  represent the geometric factors  $\frac{\partial \xi}{\partial x}$ ,  $\frac{\partial \xi}{\partial y}$ ,  $\frac{\partial \eta}{\partial x}$ , and  $\frac{\partial \eta}{\partial y}$ , respectively, and their values at each node  $(\xi_k, \eta_m)$ .

The surface integration in Eq. (34) is in fact the one-dimensional integration on each face of the local element:

$$\mathbf{R}(\bar{f}_\alpha^N) = \sum_{s=1}^4 \sum_{k=0}^N \mathcal{R}_k^s \{ (\mathbf{n} \cdot \mathbf{e}_\alpha) [(\bar{f}_\alpha^N)_{ij} - (\bar{f}_\alpha^N)_{ij}^+] \} w_k J_k^s, \quad (38)$$

where  $\mathcal{R}_k^s \{ \cdot \}$  extracts the information of  $\{ \cdot \}$  at the nodes situated on each face of the local element for the face number  $s$  and  $J_k^s$  is the surface Jacobian at the nodes on each face. To define the unit normal vector  $\mathbf{n}$  corresponding to the face in the reference domain  $I$  with respect to  $\xi$  and  $\eta$ , i.e.,  $\mathbf{n}_\xi$  and  $\mathbf{n}_\eta$ ,

respectively, we consider the infinitesimal displacement  $(x, y)$  in the tangential direction along the boundary  $\partial\Omega^e$ , which can be written as

$$\epsilon_\xi = \left( \frac{\partial x}{\partial \xi}, \frac{\partial y}{\partial \xi} \right) d\xi, \quad \text{and} \quad \epsilon_\eta = \left( \frac{\partial x}{\partial \eta}, \frac{\partial y}{\partial \eta} \right) d\eta. \quad (39)$$

From the fact that  $\frac{\partial \xi}{\partial x} \frac{\partial x}{\partial \eta} + \frac{\partial \xi}{\partial y} \frac{\partial y}{\partial \eta} = \frac{\partial \eta}{\partial x} \frac{\partial x}{\partial \xi} + \frac{\partial \eta}{\partial y} \frac{\partial y}{\partial \xi} = 0$  in Eq. (32) and the relation in Eq. (31), we can obtain the normal vectors as

$$\hat{\mathbf{n}}_\xi = \left( \frac{\partial \xi}{\partial x}, \frac{\partial \xi}{\partial y} \right) = \frac{1}{J} \left( \frac{\partial y}{\partial \eta}, -\frac{\partial x}{\partial \eta} \right), \quad \hat{\mathbf{n}}_\eta = \left( \frac{\partial \eta}{\partial x}, \frac{\partial \eta}{\partial y} \right) = \frac{1}{J} \left( -\frac{\partial y}{\partial \xi}, \frac{\partial x}{\partial \xi} \right) \quad (40)$$

so that the unit normal vectors can be defined as  $\mathbf{n}_\xi = \frac{\hat{\mathbf{n}}_\xi}{|\hat{\mathbf{n}}_\xi|}$  and  $\mathbf{n}_\eta = \frac{\hat{\mathbf{n}}_\eta}{|\hat{\mathbf{n}}_\eta|}$ . The infinitesimal lengths along the face on  $\partial\Omega^e$  corresponding to  $\xi$  and  $\eta$  are

$$dl = |\epsilon_\xi| = \left| \left( \frac{\partial x}{\partial \xi}, \frac{\partial y}{\partial \xi} \right) \right| d\xi \quad \text{and} \quad dl = |\epsilon_\eta| = \left| \left( \frac{\partial x}{\partial \eta}, \frac{\partial y}{\partial \eta} \right) \right| d\eta, \quad (41)$$

respectively, and thus their associated surface Jacobians  $J^s$  are  $\left| \left( \frac{\partial x}{\partial \xi}, \frac{\partial y}{\partial \xi} \right) \right|$  and  $\left| \left( \frac{\partial x}{\partial \eta}, \frac{\partial y}{\partial \eta} \right) \right|$ , respectively.

The semidiscrete scheme for Eq. (15) in a local domain  $\Omega^e$  can be written in matrix form as

$$\frac{d\mathbf{f}_\alpha}{dt} + \mathbf{M}^{-1} \mathbf{D} \mathbf{f}_\alpha = \mathbf{M}^{-1} \mathbf{R} \mathbf{f}_\alpha, \quad (42)$$

where  $\mathbf{f}_\alpha = [\bar{f}_\alpha^N]_{ij}$  is a solution vector,  $\mathbf{D} = e_{\alpha x} \mathbf{D}_x + e_{\alpha y} \mathbf{D}_y$ , and  $\mathbf{R}$  is the surface integration acting on the boundary nodes on each face of the local element.

### 2.2.6 Eigenvalues of the SEDG Operator

The semidiscrete SEDG scheme in Eq. (42) can be expressed in a simple form as

$$\frac{d\mathbf{f}_\alpha}{dt} = \mathbf{L} \mathbf{f}_\alpha, \quad (43)$$

where  $\mathbf{L} = \mathbf{M}^{-1}(-\mathbf{D} + \mathbf{R})$  is the spatial operator. To obtain a fully discrete scheme, we need to choose a method for integrating the system of the ordinary differential equations Eq. (43) in time. Let us denote the eigenvalues of the

spatial operator as  $\sigma$ , satisfying  $\mathbf{L}\mathbf{f}_\alpha = \sigma\mathbf{f}_\alpha$ . For a fully discrete scheme to be stable, the real part of the eigenvalues must be  $\text{Re}(\sigma) \leq 0$ . Figure 1 shows the eigenvalue spectrums of the spatial advection operator of the SEDG approximation for the central and Lax-Friedrichs fluxes with periodic and wall boundary conditions. A uniform spectral element mesh is used with the number of elements  $E = 3 \times 3$  and the approximation order  $N = 5$ .

For the case with periodic boundary conditions, all the eigenvalues of the advection operator with the central flux fall on the imaginary axis, while the eigenvalues of the advection operator for the Lax-Friedrichs flux are distributed in the negative half-plane. In Figs. 1(a) and (b), the maximum values of  $\text{Re}(\sigma)$  indicate machine precision for both central and Lax-Friedrichs fluxes. This result indicates that one can choose the time-stepping scheme whose stability region includes the imaginary axis or negative half-plane for periodic problems.

For the case with wall boundary conditions, we observe some positive eigenvalues for the advection operator with the central flux. Fig. 1(c) shows that the maximum value of  $\text{Re}(\sigma)$  is positive. Numerical solutions associated with the positive eigenvalues can grow dramatically in time, resulting in instability. Thus, central flux is not suitable for problems with wall boundary conditions. The spatial operator with the Lax-Friedrichs flux for wall boundary conditions has all the eigenvalues in the negative half-plane with a maximum value of  $\text{Re}(\sigma)$  at machine precision, shown in Fig. 1(d). Thus one can choose time-stepping scheme whose stability region includes the negative half-plane for the Lax-Friedrichs flux.

### 2.2.7 Time Stepping Method

For time integration, we choose the fourth-order, 5-stage, low-storage Runge-Kutta method defined below, whose stability region is slightly larger and with less memory than those of the classical Runge-Kutta (RK) methods:

$$\begin{aligned}
u_0 &= \mathbf{f}_\alpha^n & (44) \\
\text{for } j &= 1, \dots, 4 \\
\mathbf{K}_j &= a_j K_{j-1} + \delta t \mathbf{L}(u_j, (n + c_j)\delta t) \\
u_j &= u_{j-1} + b_j \mathbf{K}_j \\
\mathbf{f}_\alpha^{n+1} &= u_4,
\end{aligned}$$

where  $a_j, b_j$ , and  $c_j$  are given constants and

$$\begin{aligned}
\mathbf{K}_1 &= \mathbf{L}(\mathbf{f}_\alpha^n, t) = \mathbf{L}_n, \\
\mathbf{K}_2 &= \mathbf{L}(\mathbf{f}_\alpha^n + 0.5\delta t \mathbf{K}_1, t + 0.5\delta t),
\end{aligned} \tag{45}$$

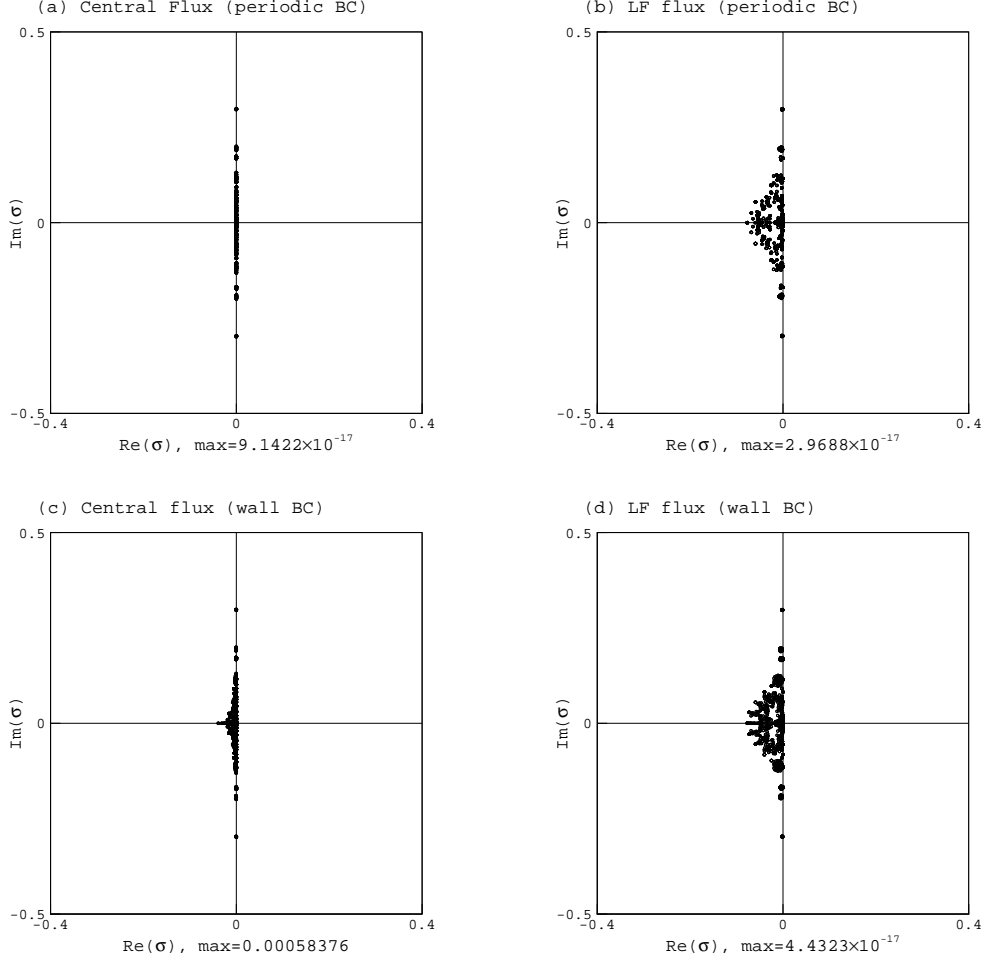


Fig. 1. Eigenvalue spectra of the spatial advection operator based on the SEDG approximation with  $E = 9$ ,  $N = 5$  for (a) central flux with periodic boundary (b) Lax-Friedrichs flux with periodic boundary (c) central flux with wall boundary (d) Lax-Friedrichs flux with wall boundary conditions.

$$\begin{aligned}\mathbf{K}_3 &= \mathbf{L}(\mathbf{f}_\alpha^n + 0.5\delta t \mathbf{K}_2, t + 0.5\delta t), \\ \mathbf{K}_4 &= \mathbf{L}(\mathbf{f}_\alpha^n + \delta t \mathbf{K}_3, \mathbf{t} + \delta t).\end{aligned}$$

The time stepping of our SEDG-LBM algorithm is summarized as follows:

- (1) Initialize density and velocity and compute the equilibrium function;
- (2) Compute collision step;
- (3) Compute advection step; impose boundary conditions through the flux;
- (4) Compute time integration with the fourth-order RK time stepping;
- (5) Compute updated density, velocity, and vorticity.

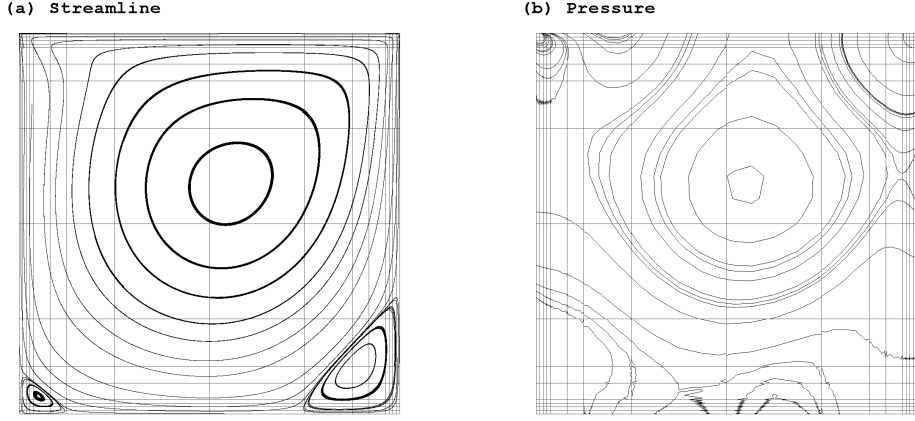


Fig. 2. Streamlines and pressure contours of the cavity flow at  $Re = 400$  with the central flux for  $E = 256$ ,  $N = 5$  with the total grids  $\mathcal{N} = (N + 1)^2 E$ .

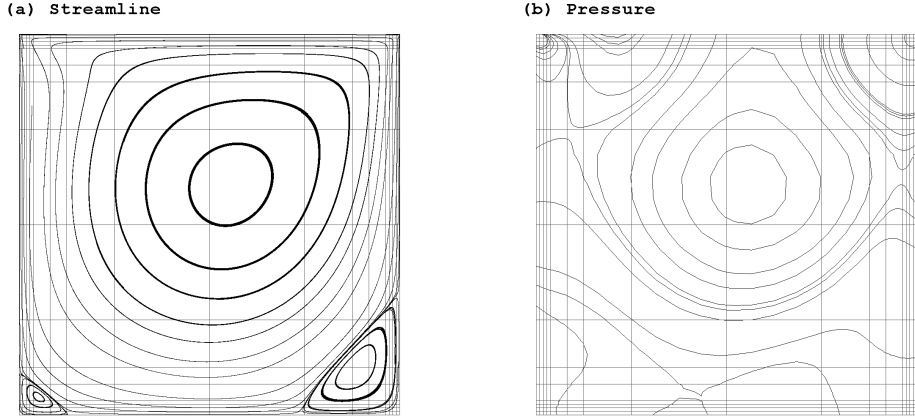


Fig. 3. Streamlines and pressure contours of the cavity flow at  $Re = 400$  with the Lax-Friedrichs flux for  $E = 256$ ,  $N = 5$  with the total grids  $\mathcal{N} = (N + 1)^2 E$ .

### 3 Computational Results

We demonstrate benchmark problems on lid-driven cavity flows and flows past an impulsively started cylinder.

#### 3.1 Lid-Driven Cavity Flow

Steady-state flows inside a square lid-driven cavity are simulated by using our SEDG-LBM described in the previous section. The Reynolds number of the lid-driven cavity flow is  $UH/\nu$ , where  $U$  is the velocity of the lid,  $H$

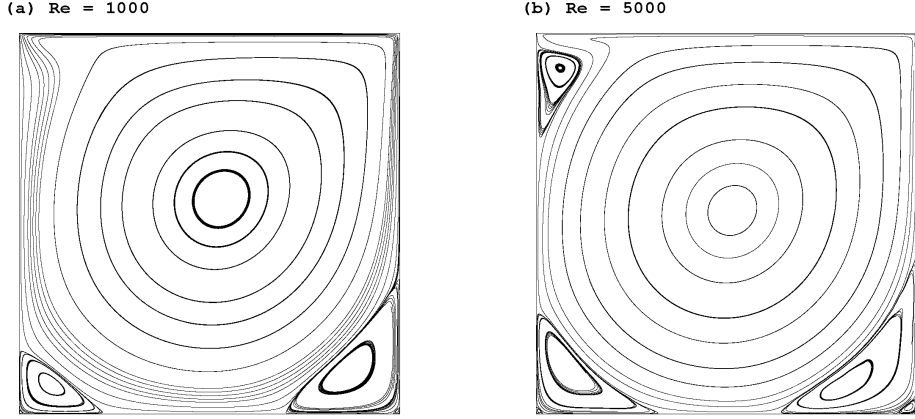


Fig. 4. Streamlines of the cavity flow at (a)  $Re = 1000$  and (b)  $Re = 5000$  with the Lax-Friedrichs flux for  $E = 256$  and  $N = 5$ , with the total grids  $\mathcal{N} = (N + 1)^2 E$ .

the length of the lid, and  $\nu$  the kinematic viscosity. The initial velocity  $\mathbf{u}$  is  $(u_x, u_y) \equiv (0, 0)$ , and the initial density  $\rho \equiv 1$ . At  $t > 0$ , we let the top lid move at the velocity  $\mathbf{u}_b = (u_x, u_y) = (Ma * c_s, 0)$  with a Mach number  $Ma = 0.1$ . The velocity of the top lid is imposed through the numerical flux as described in Section 2.2.3.

Figs. 2 and 3 show the streamlines and pressure contours of the cavity flows at  $Re = 400$  with the central and Lax-Friedrichs fluxes, respectively, including a nonuniform spectral element mesh with  $E = 256$ . We used the polynomial order of  $N = 5$  and a timestep  $\delta t$  such that  $CFL = \frac{\min_{\alpha} |\mathbf{e}_{\alpha}| \delta t}{\Delta \mathbf{x}_{\min}} = 0.4$ , where  $\Delta \mathbf{x}_{\min}$  is the minimum grid spacing. The streamlines for the two numerical fluxes are almost indistinguishable, but the pressure contours for the central flux exhibit oscillations in the lower section of the cavity.

The oscillations with the central flux become severe as  $Re$  increases, and the simulation becomes unstable at  $Re = 1000$  with the given mesh resolution. This instability is due to the effect of positive eigenvalues associated with the central flux when it is applied to wall boundary conditions (see Section 2.2.6). Thus, for  $Re \geq 1000$ , we demonstrate the results obtained from the Lax-Friedrichs flux. Fig. 4 shows the streamlines of the cavity flows at  $Re = 1000$  and  $Re = 5000$  with the Lax-Friedrichs flux.

Fig. 5 demonstrates the nondimensional horizontal velocity  $u_x/U$  along the mid-vertical line of the cavity  $y/H$  for  $Re = 400, 1000, 3200$ , and  $5000$  from our SEDG-LBM simulations, keeping the mesh resolution constant as in Figs. 2-3 with the total number of grids  $\mathcal{N} = (N + 1)^2 E = 36 \times 256$ . A good agreement at high  $Re$  is particularly notable with less resolution when compared to the Ghia et al.'s simulations [36] using an implicit multigrid method. In particular, for  $Re = 1000$ , the resolution of our SEDG-LBM is  $\mathcal{N} = 9,216$ , whereas the



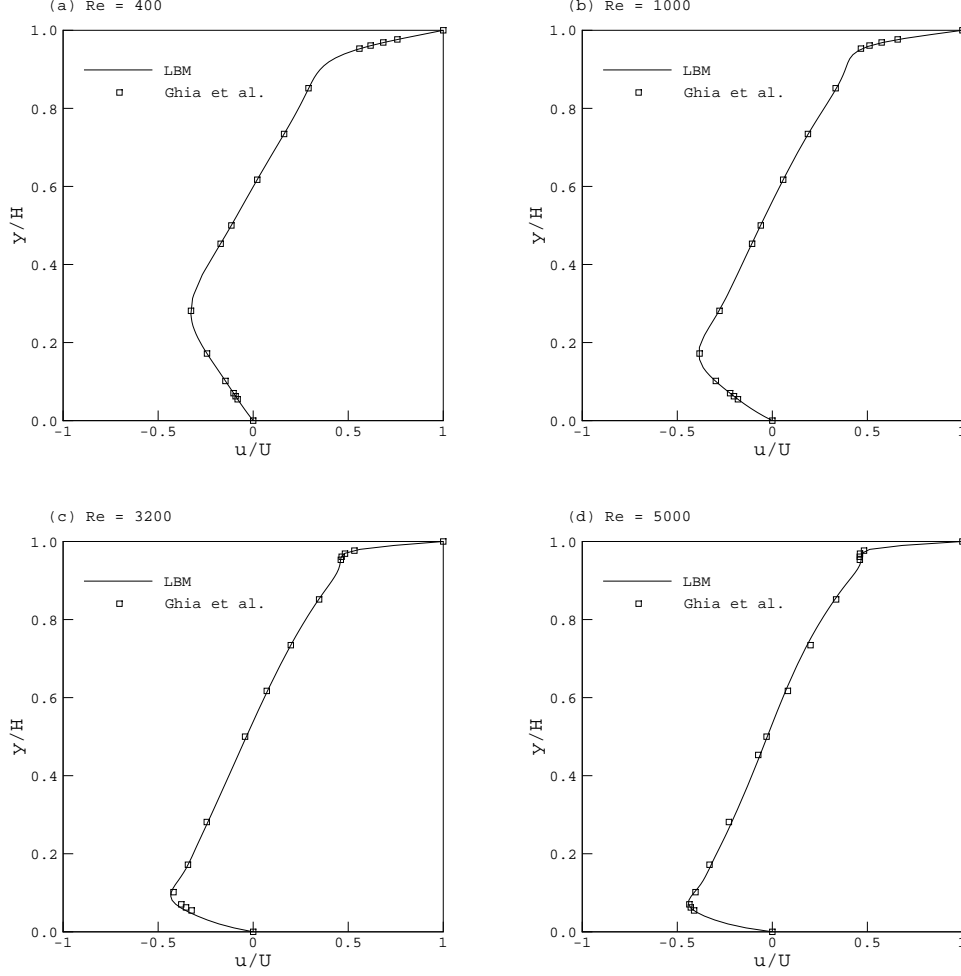


Fig. 5. Nondimensional horizontal velocity ( $u/U$ ) along mid-vertical line for  $Re = 400, 1000, 3200$ , and  $5000$ . Lines represent our SEDG-LBM results, and square dots represent the results by an implicit multigrid method by Ghia et al. [36].

total number of grids in [36] is  $129 \times 129 = 11,641$ .

### 3.2 Flow Past an Impulsively Started Cylinder

In this section, time evolution of flows around an impulsively started circular cylinder is considered, and boundary-layer development, separation, pressure forces, and drag forces are studied in detail. The computational results will be compared mainly with those from the vortex method and the spectral element method associated with the incompressible Navier-Stokes equations [37,38].

High-resolution simulations are necessary at high  $Re$  to adequately resolve the singular character of the flow at early times and to resolve the details of the separation process [39–41]. At  $t > 0$ , it is assumed that a potential

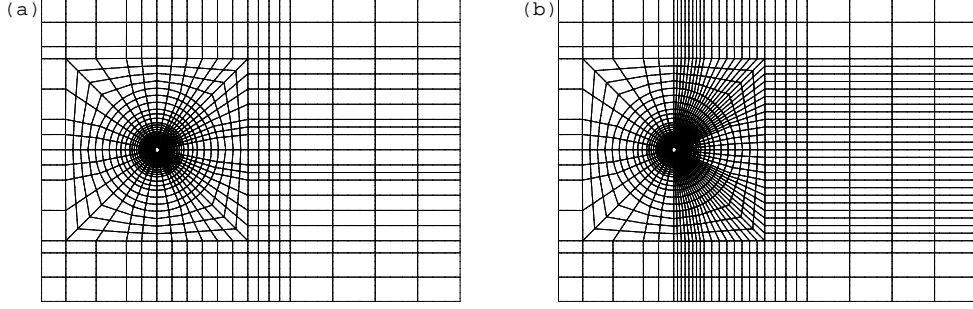


Fig. 6. Spectral element mesh with around a circular cylinder with (a)  $E = 2,208$  and (b)  $E = 3,758$ . (c) Close-up view around the cylinder for  $E = 3,758$ . Cylinder diameter  $D = 1.0$ , and computational domain  $\Omega = [-19, 50] \times [-25, 25]$ .

flow exists, and a slip velocity (vortex sheet of zero thickness) is observed on the surface of the body. Numerical schemes encounter difficulties in resolving the initially developed thin boundary layers associated with impulsive starts and in computing accurately quantities such as the drag coefficient. In our formulation the initial velocity at  $t = 0$  is zero, and for the effect of impulsive start at  $t > 0$  we impose the velocity of  $\mathbf{u}_b = (u_x, u_y) = (Ma * c_s, 0)$  around the computational domain boundaries and  $\mathbf{u}_b = (u_x, u_y) = (0, 0)$  on the surface of the cylinder. The boundary conditions are imposed weakly through the numerical flux as described in Section 2.2.3.

The Reynolds number of the flow is

$$\frac{U_\infty D}{\nu}, \quad (46)$$

where  $U_\infty$  is the uniform inlet velocity and  $D$  is the diameter of the cylinder. The nondimensional time  $T$  is based on the radius of the cylinder:

$$\frac{2U_\infty t}{D}. \quad (47)$$

Computations are carried out for  $Re = 550$  and  $9500$  with  $CFL=0.4$ . Fig. 6

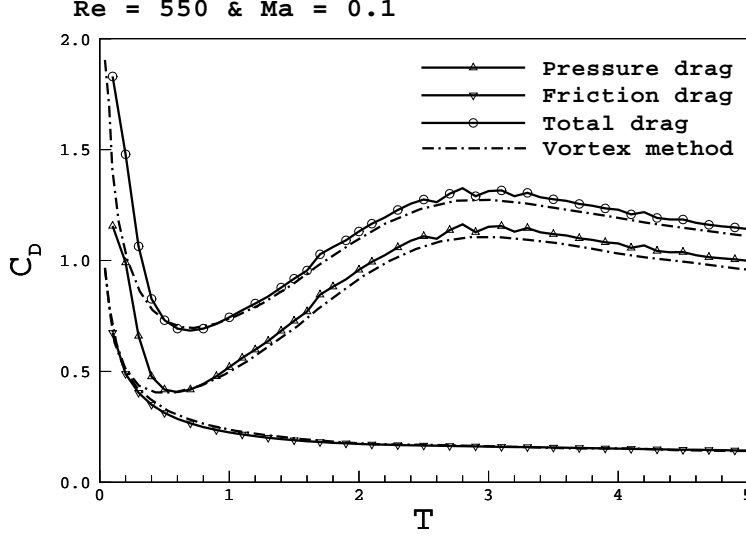


Fig. 7. Time evolution of the drag coefficients for  $Re = 550$  and  $Ma = 0.1$  with  $E = 2,208$ ,  $N = 5$ , and  $\mathcal{N} = 6^2 \times 2,208$  for the SEDG-LBM. Dash-dotted line presents the results from the vortex method by Koumoutsakos and Leonard [37].

shows a spectral element mesh with  $E = 2,208$ . The total drag force on the cylinder,  $\bar{\mathbf{F}}_t$ , is

$$\bar{\mathbf{F}}_p + \bar{\mathbf{F}}_f, \quad (48)$$

where  $\bar{\mathbf{F}}_p$  is the force due to pressure and  $\bar{\mathbf{F}}_f$  the force due to friction. The total drag coefficient of the cylinder,  $C_D$ , is

$$\frac{\bar{\mathbf{F}}_t \cdot \mathbf{i}}{\frac{1}{2}\rho_\infty U_\infty^2 D}, \quad (49)$$

where  $\mathbf{i}$  is the unit vector in the  $x$ -direction. The pressure and friction drag coefficients,  $C_{Dp}$  and  $C_{Df}$ , are defined in the similar manner.

In Fig. 7, time evolution of the pressure, friction, and total drags is compared to their time evolution with the vortex method by Koumoutsakos and Leonard [37]. At earlier times for  $T < 0.5$ , the vortex method gives a much more rapid decrease of the pressure and total drags, exhibiting a  $t^{1/2}$  singularity [40]. The friction drag coefficient of our SEDG-LBM agrees well with that obtained by the vortex method. The drag coefficients gradually recover from the sudden drop due to the impulsive start, and the SEDG-LBM results start to show good agreement with the vortex method for  $T \geq 1$ , when the effects of convection become important. As noted first in [40], the results from our SEDG-LBM shows a slower decay mainly because of its finite-compressibility effect.

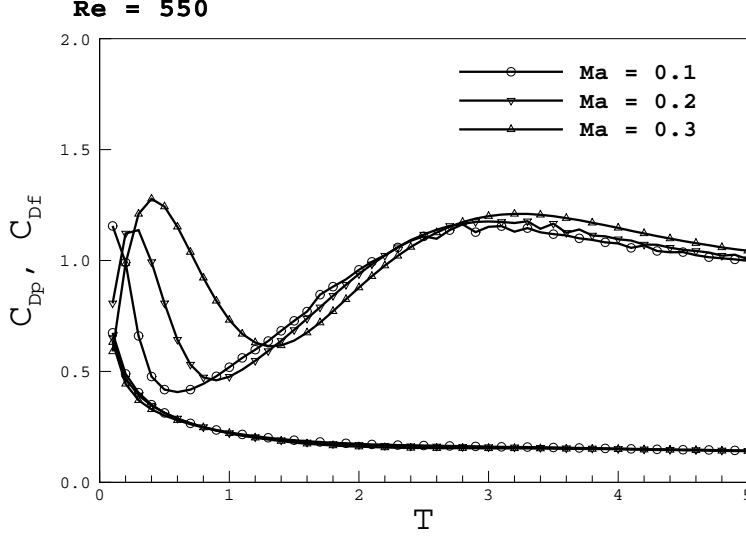


Fig. 8. Time evolution of the pressure and friction drag coefficients for  $Ma = 0.1$ ,  $0.2$ , and  $0.3$  with  $E = 2,208$ ,  $N = 5$ , and  $\mathcal{N} = 6^2 \times 2,208$  for the SEDG-LBM.

In Fig. 8, we show the drag coefficients for  $Ma=0.1$ ,  $0.2$ , and  $0.3$ . Clearly, as  $Ma$  increases, the initial decay in the pressure drag coefficient slows, and the recovery from a sudden drop due to the impulsive start is delayed. We note that the friction drag coefficient is not very sensitive to the variation of  $Ma$ . This result implies that the compressibility in LBM affects mostly the pressure field. The pressure wave originating from the impulsive start travels at a constant lattice speed of sound  $c_s$ . Since nondimensional time is measured with flow velocity  $U_\infty$ , the distance traveled by the pressure wave is inversely proportional to  $Ma$  at a given time.

Fig. 9 shows the sequence of contour plots of the nondimensional pressure wave defined as  $(p - p_\infty) / (\frac{1}{2}\rho U_\infty^2)$  for  $Ma = 0.1$  and  $Ma = 0.3$  with constant reference pressure  $p_\infty$ . Initially at  $T = 0$ , the pressure field is uniform. The pressure wave with  $Ma = 0.1$  propagates from the cylinder surface three times faster than the one with  $Ma = 0.3$  and disappears much more quickly from the cylinder. The nearly incompressible pressure field, in which the front stagnation point has the highest value and the top and bottom surfaces of cylinder have lower values, is slowly established as the pressure wave propagates outward radial direction. As the pressure at the front stagnation point is increased, the pressure drag increases until  $T < 0.5$  (Fig. 8), which takes less time for smaller  $Ma$ . Once the pressure field is recovered, the pressure drag starts to decrease and then gradually increases.

In Fig. 10, we present the results of drag coefficient in comparison with those of the vortex method [37] and the spectral element method (SEM) [38]. Our grid resolution is  $135,288$  ( $E = 3,758$ ,  $N = 5$ ) for  $Re = 9500$ ,  $Ma = 0.05$ . The results show good agreement with the results from the vortex method

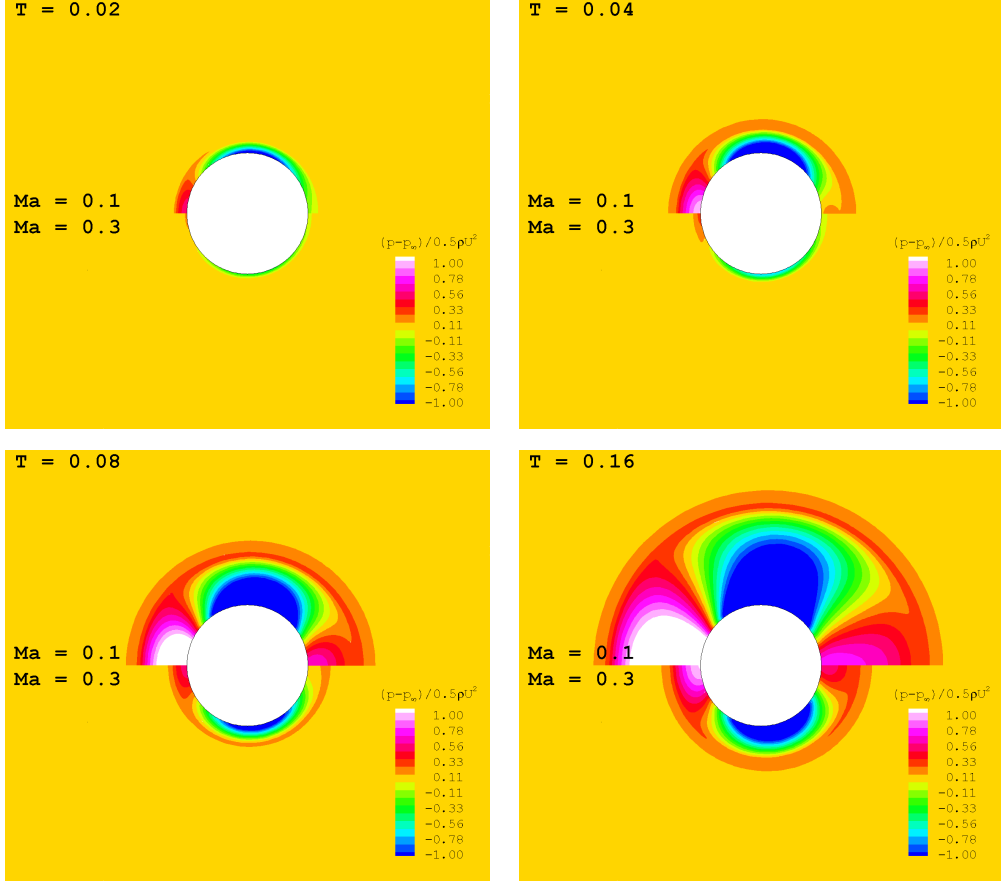


Fig. 9. Sequence of contour plots of the pressure wave  $(p - p_\infty) / (\frac{1}{2}\rho U_\infty^2)$  for  $Re = 550$  at  $T = 0.02, 0.04, 0.08$ , and  $0.16$  with  $E = 2,208$ ,  $N = 5$ , and  $\mathcal{N} = 6^2 \times 2208$  for the SEDG-LBM. Upper and lower halves represent SEDG-LBM simulations at  $Ma = 0.1$  and  $Ma = 0.3$ , respectively.

and SEM. The delay in establishing the incompressible pressure field around the cylinder contributes to the discrepancy in the pressure drag coefficients at early time between the results from SEDG-LBM, the vortex method, and SEM, as shown in Fig. 10.

Figs. 11 and 12 demonstrate the time sequence of streamlines with  $Ma = 0.1$  for  $Re = 550$  and  $Re = 9500$  at different times  $T$ . The number of spectral elements  $E = 2,208$  and the polynomial order of  $N = 5$  are used.

## 4 Conclusions

We have presented a spectral-element discontinuous Galerkin lattice-Boltzmann method for solving incompressible flows, such as the flows for a lid-driven cavity and an impulsively started cylinder. We decoupled our numerical scheme into collision and streaming steps, giving flexibility in dealing with numer-

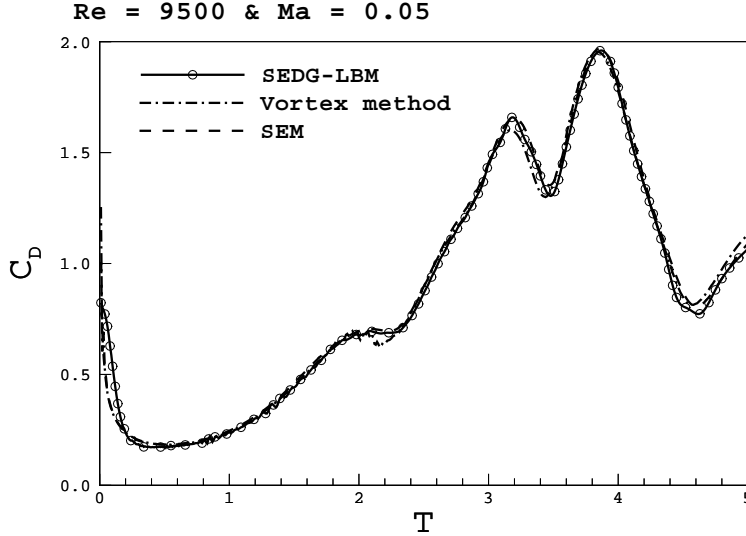


Fig. 10. Time evolution of the drag coefficients for  $Re = 9500$  and  $Ma = 0.05$  computed on a mesh with  $E = 3,758$ ,  $N = 5$ , and  $\mathcal{N} = (N + 1)^2 E = 6^2 \times 3,758 = 135,288$  for the SEDG-LBM. Dash-dotted line presents the results obtained from the vortex method [37] and dashed line from the spectral element simulations [38].

ical stability at high Reynolds numbers. In the streaming step, we used a spectral element discretization in a discontinuous Galerkin form with a fully diagonal mass matrix for solving the advection equation. We have shown the implementation to impose boundary conditions weakly through the numerical fluxes with the central and Lax-Friedrichs fluxes.

We have examined lid-driven cavity flows for  $Re=400$ – $5000$  and flows around an impulsively started cylinder for  $Re=550$ – $9500$ . Computational results show good agreement with results from previously studied methods, namely, an implicit multigrid method, a vortex method, and a spectral element method. Our method shows some delay in establishing incompressibility at the initial stage of the simulation.

## Acknowledgments

This work was partially supported by the Office of Advanced Scientific Computing Research, Office of Science, U.S. Department of Energy, under Contract DE-AC02-06CH11357, and partially by the National Science Foundation grant DMS-0811046. We thank Paul Fischer for his helpful discussions and providing his drag coefficient data for SEM and the vortex method.

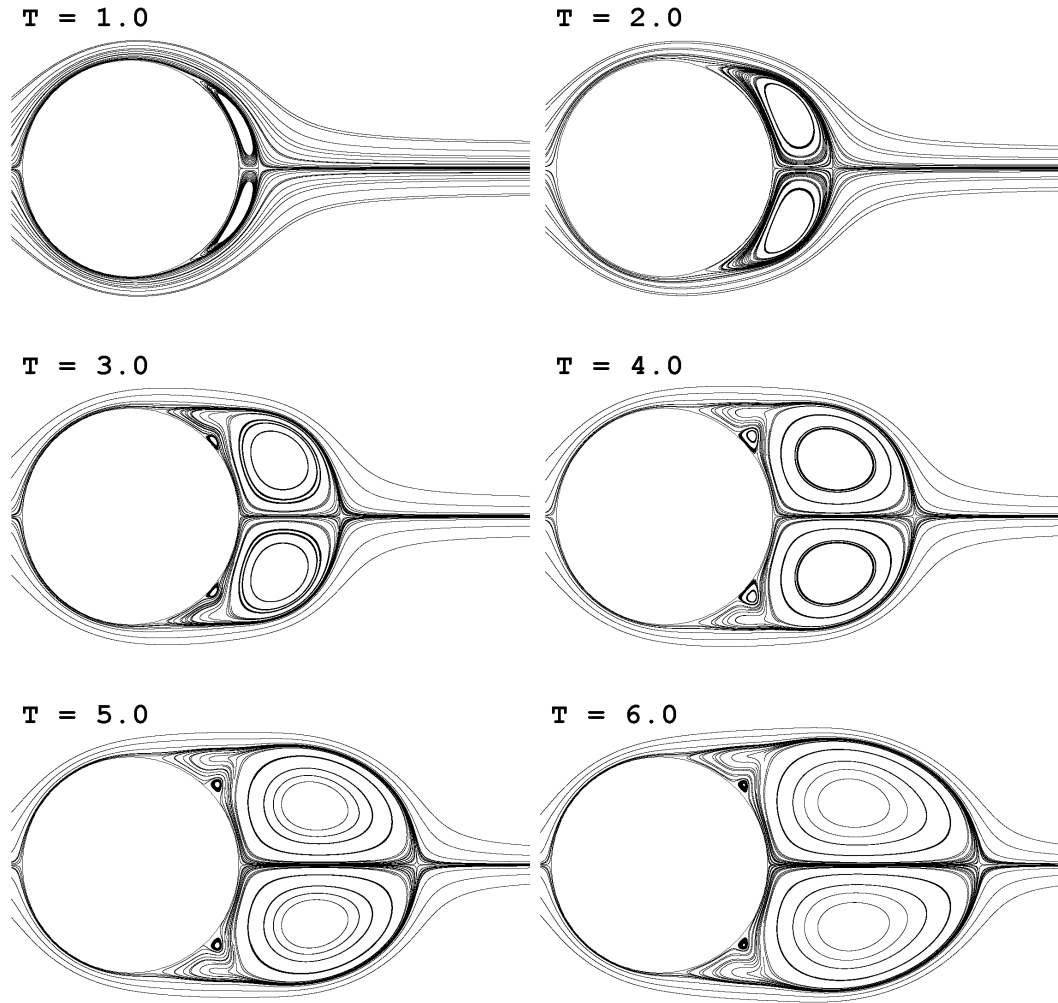


Fig. 11. Time evolution of streamlines at  $Re = 550$  and  $Ma = 0.1$ ;  $E = 2,208$ ,  $N = 5$  and  $\mathcal{N} = (N + 1)^2 E$ .

## References

- [1] D.A. Wolf-Gladrow, Lattice-gas cellular automata and lattice Boltzmann models: An introduction, *Lecture Notes in Mathematics* (Springer, Berlin, 2000) 1725.
- [2] S. Succi, The lattice Boltzmann equation: For fluid dynamics and beyond, Oxford University Press, 2001.
- [3] M.C. Sukop, D.T. Thorne, Lattice Boltzmann modeling: An introduction for geoscientists and engineers (Springer, 2007).
- [4] X. He, L.-S. Luo, Theory of the lattice Boltzmann method: From the Boltzmann equation to the lattice Boltzmann equation, *Phys. Rev. E* **53** (1997) 6811-6817.
- [5] T. Abe, Derivation of the lattice Boltzmann method by means of the discrete

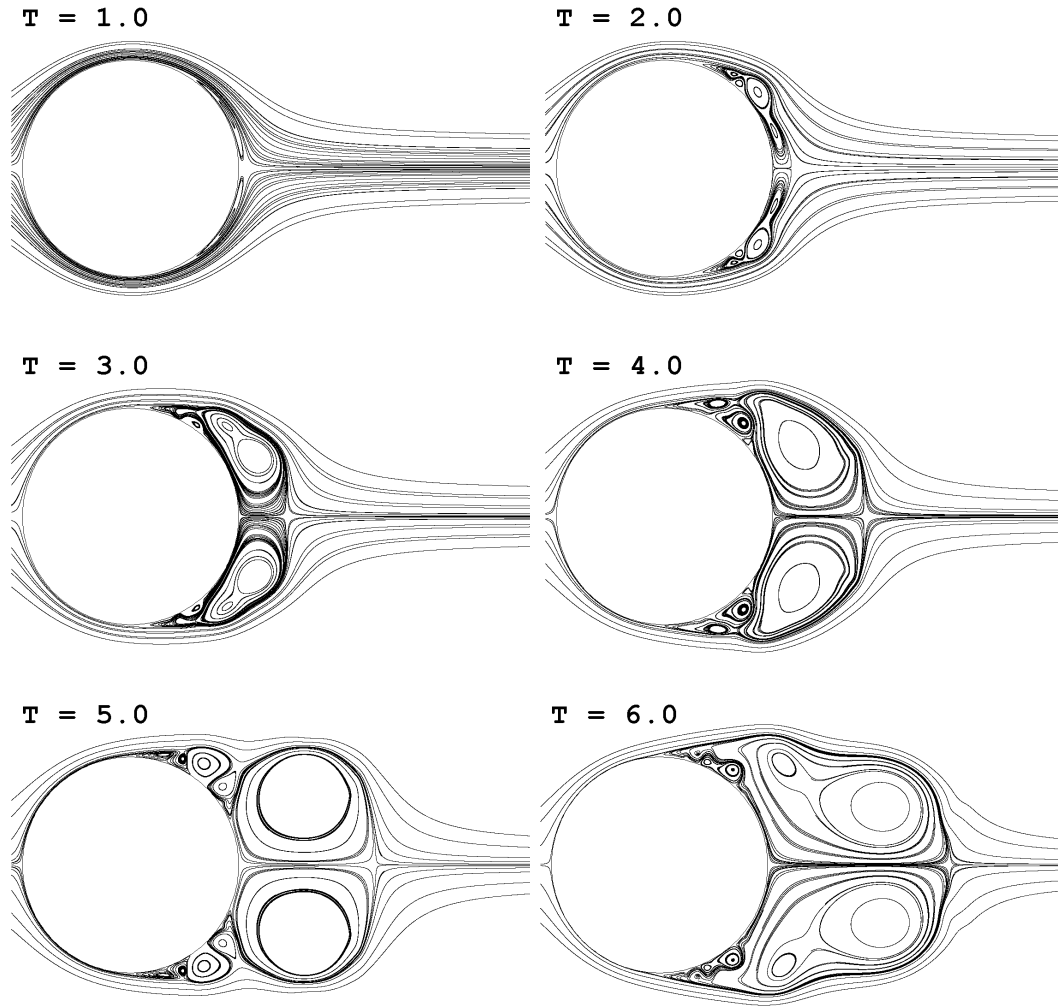


Fig. 12. Time evolution of streamlines at  $Re = 9500$  and  $Ma = 0.1$ ;  $E = 2,208$ ,  $N = 5$ , and  $\mathcal{N} = (N + 1)^2 E$ .

ordinate method for the Boltzmann equation, *J. Comput. Phys.* **131** (1997) 241.

- [6] N. Cao, S. Chen, S. Jin, D. Martinez, Physical symmetry and lattice symmetry in the lattice Boltzmann method, *Phys. Rev. E* **55** (1997) R21.
- [7] G.R. McNamara, A.L. Garcia, B.J. Alder, Stabilization of thermal lattice Boltzmann models, *J. Stat. Phys.* **81** (1995) 395.
- [8] X. He, L.-S. Luo, M. Dembo, Some progress in lattice Boltzmann method. Part I. Nonuniform mesh grids, *J. Comput. Phys.* **129** (1996) 357-363.
- [9] R. Mei, W. Shyy, On the finite difference-based lattice Boltzmann method in curvilinear coordinates, *J. Comput. Phys.* **143** (1998) 426-448.
- [10] R. Zhang, H. Chen, Y.H. Qian, S. Chen, Effective volumetric lattice Boltzmann scheme, *Phys. Rev. E* **63** (2001) 056705.



- [11] V. Sofonea, R.F. Sekerka, Viscosity of finite difference lattice Boltzmann models, *J. Comput. Phys.* **184** (2003) 422-434.
- [12] A. Bardow, I.V. Karlin, A.A. Gusev, General characteristic-based algorithm for off-lattice Boltzmann simulations, *Europhys. Lett.* **75** (2006) 434-440.
- [13] T. Lee, C.-L. Lin, L.-D. Chen, A lattice Boltzmann algorithm for calculation of the laminar jet diffusion flame, *J. Comput. Phys.* **215** (2006) 133-152.
- [14] H. Xi, G. Peng, S.-H. Chou, Finite volume lattice Boltzmann method, *Phys. Rev. E* **59** (1999) 6202.
- [15] S. Ubertini, G. Bella, S. Succi, Unstructured lattice Boltzmann method: Further development, *Phys. Rev. E* **68** (2003) 016701.
- [16] M. Stiebler, J. Tölke, M. Krafczyk, An upwind discretization scheme for the finite volume lattice Boltzmann method, *Comput. Fluids* **35** (2006) 814-819.
- [17] F. Dubois, P. Lallemand, On lattice Boltzmann scheme, finite volumes and boundary conditions, *Prog. Comput. Fluid Dyn.* **8** (2008) 11-24.
- [18] V. Patil, K.N. Lakshmisha, Finite volume TVD formulation of lattice Boltzmann simulation on unstructured mesh, *J. Comput. Phys.* **228** (2009) 5262-5279.
- [19] T. Lee, C.-L. Lin, A characteristic Galerkin method for discrete Boltzmann equation, *J. Comput. Phys.* **171** (2001) 336-356.
- [20] T. Lee, C.-L. Lin, An Eulerian description of the streaming process in the lattice Boltzmann equation, *J. Comput. Phys.* **185** (2003) 445-471.
- [21] Y. Li, E.J. LeBoeuf, P.K. Basu, Least-squares finite-element scheme for the lattice Boltzmann method on an unstructured mesh, *Phys. Rev. E* **72** (2005) 046711.
- [22] X. Shi, J. Lin, Z. Yu, Discontinuous Galerkin spectral element lattice Boltzmann method on triangular element, *Int. J. Numer. Meth. Fluids* **42** (2003) 1249-1261.
- [23] A. Düster, L. Demkowicz, E. Rank, High-order finite elements applied to the discrete Boltzmann equation, *Int. J. Numer. Meth. Engrg.* **67** (2006) 1094-1121.
- [24] T. Lee, G.K. Leaf, Eulerian description of high-order bounce-back scheme for lattice Boltzmann equation with curved boundary, *Eur. Phys. J. Special Topics* **171** (2009) 3-8.
- [25] C. Pan, L.-S. Luo, C.T. Miller, An evaluation of lattice Boltzmann scheme for porous medium flow simulation, *Comput. Fluids* **35** (2006) 898-909.
- [26] B. Chun, A.J.C. Ladd, Interpolated boundary condition for lattice Boltzmann simulations of flows in narrow gaps, *Phys. Rev. E* **75** (2007) 066705.
- [27] J.S. Hesthaven and T. Warburton, Nodal discontinuous Galerkin methods, algorithms, analysis, and applications, *Texts in Applied Mathematics* (Springer, 2008).

- [28] X. He, Q. Zou, L.-S. Luo, M. Dembo, Analytic solutions of simple flows and analysis of nonslip boundary conditions for the lattice Boltzmann BGK model, *J. Stat. Phys.* **87** (1997) 115-136.
- [29] P.L. Bhatnagar, E.P. Gross, and M. Krook, A model for collision processes in gases. I. Small amplitude processes in charged and neutral one-component system, *Phys. Rev.* **94** (1954) 511.
- [30] Y.H. Qian, D. D’Humières, P. Lallemand, Lattice BGK models for Navier-Stokes equation, *Europhys. Lett.* **17** (1992) 479-484.
- [31] X. He, S. Chen, G.D. Doolen, A novel thermal model for the lattice Boltzmann method in incompressible limit, *J. Comput. Phys.* **146** (1998) 282-300.
- [32] F.X. Giraldo, M. Restelli, A study of spectral element and discontinuous Galerkin methods for the Navier-Stokes equations in nonhydrostatic atmospheric modeling: equation sets and test cases, *J. Comp. Phys.* **227** (2008) 3849-3877.
- [33] F.X. Giraldo, T. Warburton, A triangular discontinuous Galerkin oceanic shallow water model, *Int. J. Numer. Meth. Fluids* **56** (2008) 899-925.
- [34] M.O. Deville, P.F. Fischer, E.H. Mund, High-order methods for incompressible fluid flow, *Cambridge Monographs on Applied and Computational Mathematics* (Cambridge University Press, 2002).
- [35] J. Hesthaven, S. Gottlieb, D. Gottlieb, Spectral methods for time-dependent problems, *Volume 21 of Cambridge monographs on applied and computational mathematics* (Cambridge University Press, 2007).
- [36] U. Ghia, K.N. Ghia, C.T. Chin, High  $Re$  solutions for incompressible flow using the Navier-Stokes equation and multigrid methods, *J. Comput. Phys.* **48** (1982) 387.
- [37] P. Koumoutsakos, A. Leonard, High-resolution simulations of the flow around an impulsively started cylinder using vortex methods, *J. Fluid Mech.* **296** (1995) 1-38.
- [38] P.F. Fischer, An overlapping Schwarz method for spectral element solution of the incompressible Navier-Stokes equations, *J. Comput. Phys.* **133** (1997) 84-101.
- [39] X.D. Niu, Y.T. Chew, C. Shu, Simulation of flows around an impulsively started circular cylinder by Taylor series expansion- and least squares-based lattice Boltzmann method, *J. Comput. Phys.* **188** (2003) 176-193.
- [40] Y. Li, R. Shock, R. Zhang, H. Chen, Numerical study of flow past an impulsively started cylinder by the lattice-Boltzmann method, *J. Fluid Mech.* **519** (2004) 273-300.
- [41] A. Dupuis, P. Chatelain, P. Koumoutsakos, An immersed boundary-lattice-Boltzmann method for the simulation of the flow past an impulsively started cylinder, *J. Comput. Phys.* **227** (2008) 4486-4498.

The submitted manuscript has been created by UChicago Argonne, LLC, Operator of Argonne National Laboratory ("Argonne"). Argonne, a U.S. Department of Energy Office of Science laboratory, is operated under Contract No. DE-AC02-06CH11357. The U.S. Government retains for itself, and others acting on its behalf, a paid-up nonexclusive, irrevocable worldwide license in said article to reproduce, prepare derivative works, distribute copies to the public, and perform publicly and display publicly, by or on behalf of the Government.